Reyes-Canales, M., Rodriguez, G., Yusifbayov, J., & van der Baan, M. (2022). The Rise, Peak and Decline of the Seismic Hazard Related to Hydraulic Fracturing Activities in the Duvernay Play, Fox Creek Area, Alberta. *Journal of Geophysical Research: Solid Earth*, *127*(1), [e2021JB023060]. https://doi.org/10.1029/2021JB023060

JGR Solid Earth

RESEARCH ARTICLE
10.1029/2021JB023060

Special Section:
Understanding and anticipating Induced Seismicity: From mechanics to seismology

The Rise, Peak and Decline of the Seismic Hazard Related to Hydraulic Fracturing Activities in the Duvernay Play, Fox Creek Area, Alberta

Mauricio Reyes Canales[1], German Rodriguez-Pradilla[2], Javad Yusifbayov[1], and Mirko van der Baan[3]

[1]Alberta Geological Survey, Alberta Energy Regulator, Edmonton, AB, Canada, [2]School of Earth Sciences, University of Bristol, Bristol, UK, [3]Department of Physics, University of Alberta, Edmonton, AB, Canada

Key Points:

- The annual likelihood of events $M > 4$ in the Fox Creek area has consistently declined since 2015, in contrast with increasing activities
- Induced seismicity is characterized by two regions with largely different b-values and seismic hazard but similar earthquake numbers
- The minimum injection volume to trigger seismicity increases over the years, indicating successful mitigation strategies

Supporting Information:

Supporting Information may be found in the online version of this article.

Correspondence to:

M. Reyes Canales,
mauricio.canales@aer.ca

Citation:

Reyes Canales, M., Rodriguez-Pradilla, G., Yusifbayov, J., & van der Baan, M. (2022). The rise, peak and decline of the seismic hazard related to hydraulic fracturing activities in the Duvernay play, Fox Creek area, Alberta. *Journal of Geophysical Research: Solid Earth*, *127*, e2021JB023060. https://doi.org/10.1029/2021JB023060

Received 2 SEP 2021
Accepted 4 JAN 2022

Abstract We analyze the temporal evolution of the induced seismicity related to hydraulic fracturing activities in the Duvernay Formation, near Fox Creek, Alberta, Canada. For this analysis, we estimate annual Gutenberg-Richter parameters, $a(t)$- and $b(t)$- values, and then calculate the annual likelihood of earthquakes greater than magnitude $M > 4$ from 2014 to 2020. The seismic hazard near Fox Creek has consistently decreased since 2015, from a 95% probability of an earthquake greater than magnitude $M > 4$ in 2015 to 4% in 2019 and less than 1% probability in 2020. The induced seismicity in Fox Creek is characterized by two actively seismic regions with distinctive features: (a) an Eastern region (~220 events $M > 2$) with lower b-values and higher hazard; (b) a Western region (~210 events $M > 2$) with higher b-values and lower seismic hazard. In contrast, extensive regions where hydraulic fracturing is performed, particularly East of the seismic cluster, remain non-seismogenic. The overall decreasing seismic hazard, which contrasts with increasing operator activity, can be associated with (a) the intensification of hydraulic fracturing operations toward areas less susceptible to induced seismicity and (b) the reduction of seismic activity in the Eastern region, which exhibits the highest seismic hazard. We also find evidence of a minimum annual injection volume required to trigger induced seismicity in both the Western and Eastern regions. The minimum injection threshold increases over the years, implying increasingly successful mitigation strategies, likely due to regulatory implementations in the area, which has led the operators to exercise precaution in regions with significant seismic hazard and adapt treatment strategies to avoid triggering moderate magnitude size events during hydraulic fracturing stimulations.

Plain Language Summary In recent times, there has been a surge in the number of earthquakes in tectonically stable regions in North America, thought to be associated with the development of unconventional hydrocarbon plays. This is the case of the Duvernay Formation near Fox Creek, Alberta, Canada, where hydraulic fracturing activities have been associated with increasing seismicity since December 2013. Most of these events are of small magnitude, and just a portion of the hydraulic fracturing activities are associated with induced seismicity. However, induced events related to the development of shale plays could generate increasing seismic hazard in areas with low natural seismic activity, leading to growing public awareness. In this study, we analyze the seismicity near Fox Creek to determine the annual likelihood of earthquakes greater than magnitude $M > 4$. We found that the seismic hazard near Fox Creek has declined since its peak in 2015, from a 95% probability of an earthquake greater than magnitude $M > 4$ in 2015 to 4% in 2019, and less than 1% probability in 2020. There are multiple reasons for this decrease in the seismic hazard, including the migration of activities toward areas less susceptible to induced seismicity and changes in the operational practices, at least partially in response to regulatory implementations in the area.

1. Introduction

The Duvernay Formation is an unconventional tight shale play that extends through most of central Alberta, displaying a thickness ranging between 25 and 60 m (Davis & Karlen, 2013). This shale formation consists of multicyclic black organic-rich shale units and bituminous carbonates (Weissenberger & Potma, 2001). The Duvernay Formation initially acted as the source rock for many conventional reservoirs in the surrounding Leduc Formation and underlying Swan Hills Formation carbonate buildups (Rodgers, 2014). Development of hydrocarbon

resources in the Duvernay Fm. has become economically viable during the last decade (Rodgers, 2014), with hydraulic fracturing operations in the Fox Creek region beginning in 2010, with a substantial increase after 2012.

Since December 2013, induced seismicity related to hydraulic fracturing activity in the Duvernay Fm. has been recorded west of the town of Fox Creek, Alberta, Canada (Schultz et al., 2017, 2018). Subsequently, this area has become one of the most seismically active regions of the province, with over 490 events larger than magnitude $M_L >$ 2.0 between December 2013 and December 2020 (Alberta Geological Survey, 2021). Most of these events, however, are of minor magnitude. Only four earthquakes correspond to events with a magnitude greater than $M > 4.0$, with the largest event occurring in January 2016 ($M_L =$ 4.8). The induced seismicity in the Fox Creek area has been associated with the reactivation of critically stressed basement-rooted faults, displaying a strike-slip orientation (Wang et al., 2017). This observation is consistent with fault interpretations from 3-D reflection seismic data (Chopra et al., 2017; Eaton et al., 2018) and the present-day tectonic stress field in the Fox Creek area (Shen, Schmitt, & Schultz, 2019; Zhang et al., 2019).

The seismic hazard caused by induced seismicity could be higher than the natural seismic hazard, especially in areas with small-to-moderate natural background seismicity, like Fox Creek (Atkinson et al., 2015, 2016). To address these concerns, since February 2015, operators performing hydraulic fracturing in the Duvernay Fm. are mandated to monitor adjacent seismicity activities during the operations and follow the traffic light protocol (Subsurface Order No. 2, SSO No. 2, Alberta Energy Regulator, 2015). Under the traffic light protocol, operators performing hydraulic fracturing activities in the Duvernay Fm. must inform the regulator of any event larger than $M > 2$ (yellow-light event threshold), and actively implement mitigation strategies to avoid larger events. If a red-light event occurs ($M > 4$), the operator must cease operations immediately (Alberta Energy Regulator, 2015).

In this study, we analyze the temporal evolution of the seismic hazard in Fox Creek, expressed in the annual likelihood of moderate events with a magnitude greater than $M > 4$ (red-light earthquakes). This retrospective analysis is an effective way to study the evolution of the seismic hazard, which in the case of anthropogenic induced seismicity is a function of changes in industrial activity. First, we define time-dependent annual Gutenberg-Righter parameters, $a(t)$- and $b(t)$-values and calculate the annual likelihood of events $M > 4$ assuming a Poisson distribution. We found that the seismic hazard in Fox Creek has consistently declined since 2015, from a 95% probability to have an earthquake $M > 4$ in 2015 to less than 1% probability in 2020. In contrast, the peak in the number of hydraulic fracturing wells and the total volumes injected into the Duvernay Fm., SSO No. 2 area, occurred in 2018, and 2019, respectively. This consistent decrease in the likelihood of red-light events is related to the intensification of hydraulic fracturing activities in areas less susceptible to induced seismicity, reduction of activities in regions with observed higher seismic hazard, and active mitigation strategies performed by the operators to avoid moderate magnitude size events, led by regulatory implementations (SSO No. 2) in the area. First, we briefly review the relevant theory to compute the probability that an event of a certain magnitude occurs within some time frame. Then we describe the temporal and spatial evolution of observed seismicity, which we compare with annual and cumulative injection and production profiles. We end by comparing the seismic hazard and induced seismicity to pore pressure and stress profiles to examine possible causes explaining the difference in observed patterns and hazards.

2. Theory

2.1. Time-Dependent Gutenberg-Richter Parameters

The magnitude-frequency distribution of earthquakes is described by the Gutenberg-Richter (GR) distribution (Gutenberg & Richter, 1944), and it is given by:

$$\log(\lambda_m) = a - bm, \tag{1}$$

where λ_m is the rate of earthquakes with magnitudes greater than m. The b-value indicates the ratio of small and large magnitude events and the a-value is related to the number N_0 of earthquakes with a magnitude larger than $m > 0$ per time unit. The value N_0 it is given by:

$$N_0 = 10^a. \tag{2}$$

Reyes Canales and van der Baan (2019) defined time-dependent GR parameters, $a(t)$- and $b(t)$ -values, and derived analytical expressions required in Probabilistic Seismic Hazard Analysis for non-stationary seismic sources. Some relevant expressions for the seismic hazard analysis include the rate of exceedance $\lambda_{\text{exc}}(m \geq m_j, t)$ for a given magnitude level m_j. For a non-stationary source, the rate of exceedance $\lambda_{\text{exc}}(m \geq m_j, t)$ is given by (Reyes Canales & van der Baan, 2019):

$$\lambda_{\text{exc}}(m \geq m_j; t) = P(m_j \leq m \leq M_{\text{max}}; t) N(M_{\text{min}} \leq m \leq M_{\text{max}}; t), \tag{3}$$

where $P(m_j \leq m \leq M_{\text{max}}; t)$ is the time-varying probability of occurrence for a magnitude m occurring in a range $m = [m_j \leq m \leq M_{\text{max}}]$, and $N(M_{\text{min}} \leq m \leq M_{\text{max}}; t)$ is the total expected number of earthquakes in the range $m = [M_{\text{min}} \leq m \leq M_{\text{max}}]$. The variables M_{min} and M_{max} represent the minimum and maximum magnitudes considered, respectively. The probability $P(m_j \leq m \leq M_{\text{max}}; t)$ is defined as:

$$P(m_j \leq m \leq M_{\text{max}}; t) = F_M(M_{\text{max}}; t) - F_M(m_j; t), \tag{4}$$

where $F_M(m; t)$ denotes the cumulative distribution function for a magnitude m, and is given by:

$$F_M(m; t) = \frac{1 - 10^{-b(t)(m - M_{\text{min}})}}{1 - 10^{-b(t)(M_{\text{max}} - M_{\text{min}})}}. \tag{5}$$

In this expression, $b(t)$ corresponds to the time-dependent b-value in the Gutenberg-Richter relationship. On the other hand, the total expected number of earthquakes $N(M_{\text{min}} \leq m \leq M_{\text{max}}; t)$ in the range $m = [M_{\text{min}} \leq m \leq M_{\text{max}}]$, it is defined as:

$$N(M_{\text{min}} \leq m \leq M_{\text{max}}; t) = 10^{a(t) - b(t) M_{\text{min}}} - 10^{a(t) - b(t) M_{\text{max}}}, \tag{6}$$

where $a(t)$ corresponds to the time-dependent a-value in the Gutenberg-Richter relationship. For simplicity, we assume annual $a(t)$-and $b(t)$-values in this study.

2.2. Non-Stationary Poisson Distribution

The Poisson distribution is typically used to describe the number of events within a certain time interval for stationary earthquake rates (Baker, 2008; Cornell, 1968). The stationary Poisson distribution is defined by (Cornell, 1968):

$$P[N = n; t_a, t_b] = \frac{\lambda^n (t_b - t_a)^n e^{-\lambda(t_b - t_a)}}{n!}, \tag{7}$$

where $P[N = n; t_a, t_b]$ is the probability of n occurrences in a time interval $\Delta t = t_b - t_a$, for start and end times t_a and t_b respectively, and λ is the rate of occurrence of events per unit time duration. By definition $0! = 1$. On the other hand, the probability $P[N > 0; t_a, t_b]$ of at least one event happening in a time interval $\Delta t = t_b - t_a$ is given by:

$$P[N > 0; t_a, t_b] = 1 - e^{\lambda(t_b - t_a)}. \tag{8}$$

The non-stationary Poisson model has a rate of occurrence that varies with time, and the mean $m_\lambda(t_a, t_b)$ of the time-dependent rate is used instead of the constant rate of occurrence λ. The non-stationary Poisson distribution is defined as (Sigman, 2013):

$$P[N = n; t_a, t_b] = \frac{m_\lambda(t_a, t_b)(t_b - t_a)^n e^{-m_\lambda(t_a, t_b)(t_b - t_a)}}{n!}, \tag{9}$$

where $m_\lambda(t_a, t_b)$ is the mean of the time-varying rate of occurrence $\lambda(t)$ in the time interval $\Delta t = t_b - t_a$, and it is defined as (Sigman, 2013):

$$m_\lambda(t_a, t_b) = \frac{\int_{t_a}^{t_b} \lambda(s) ds}{(t_b - t_a)}. \tag{10}$$

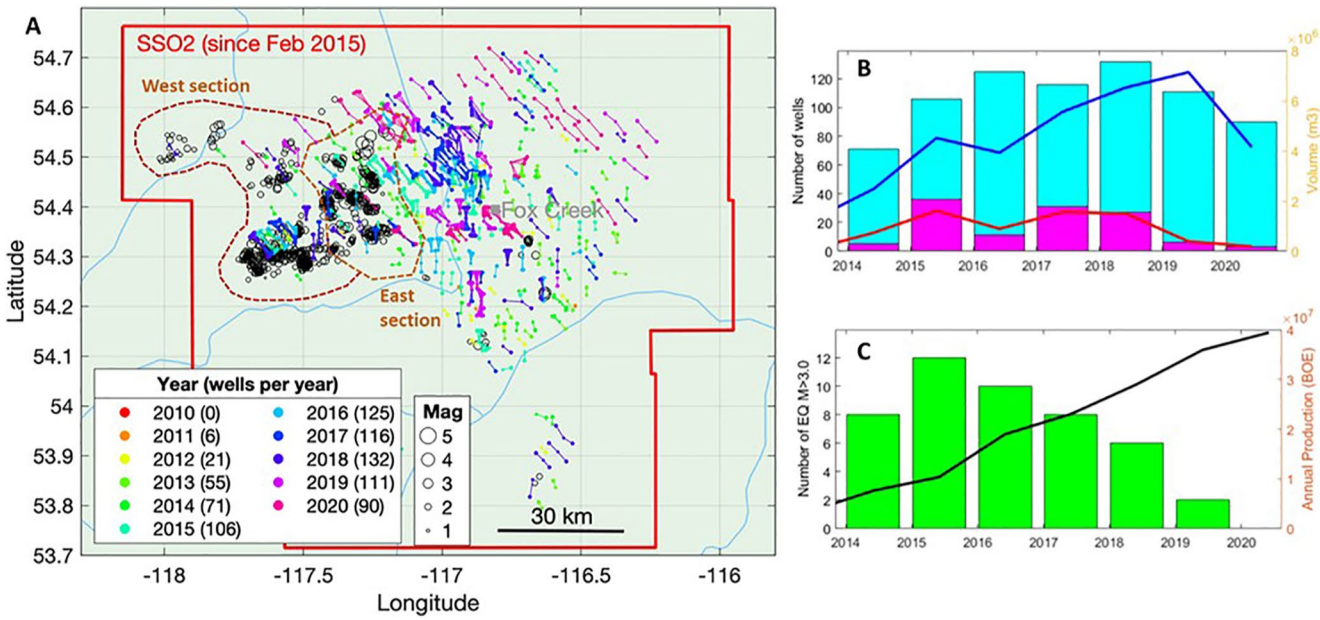

Figure 1. (a) Location map of the wells hydraulic fractured inside the Duvernay Zone designated in the Subsurface Order No. 2 (SSO No. 2, Alberta Energy Regulator, 2015) between 2010 and 2020, and the earthquakes reported in the same period. The approximate boundaries of the Eastern and Western sections of the seismic cluster are shown by the dashed contours. (b) Total number of hydraulic fracturing wells in the Duvernay Formation, SSO No. 2 area (blue bars), and the number of positively correlated seismogenic wells (magenta bars) per year. The total hydraulic fracturing volumes injected per year from all wells (blue line) and seismogenic wells (red line) are also shown. (c) Annual number of earthquakes larger than magnitude $M > 3$ (green bars) and annual hydrocarbon production from the Duvernay Fm., SSO No. 2 area (black line).

For instance, the rate of occurrence $\lambda(t)$ could be replaced by the time-dependent rate of exceedance $\lambda_{\text{exc}}(m \geq m_j; t)$ for a given magnitude, Equation 3. Therefore, by estimating the annual changes in the non-stationary rate of exceedance $\lambda_{\text{exc}}(m \geq m_j; t)$ and still assuming a Poisson distribution, it is possible to calculate the likelihood of n earthquakes with magnitude larger than m_j per year. See Reyes Canales and van der Baan (2019) for additional background.

3. Data and Methods

We analyze the Alberta Geological Survey (AGS) catalog from December 2013 to December 2020, considering only the earthquakes in the area defined by SSO No. 2 around Fox Creek (See Figure 1). The AGS catalog is a focused and regionally enriched catalog (Stern et al., 2013), and is available online via the Seismicity Dashboard on the AGS website (Alberta Geological Survey, 2021). The earthquake catalog in the Fox Creek area contains 1380 earthquakes in the magnitude range $M = [0, 4.8]$. Prior to December 2013, only 4 events were recorded in the Fox Creek area between 2007 and 2012. The magnitude of completeness varies over time as described below.

The operational data analyzed in this study is focused on the volumes injected during the hydraulic fracturing activities in the Duvernay Fm., SSO No. 2 area (see Figure 1). The tour reports containing hydraulic fracturing parameters for each well are available through the Alberta Energy Regulator. The hydraulic fracturing activities in the Duvernay Fm. started in late 2010 near Fox Creek. However, induced seismicity related to hydraulic fracturing activities did not start until December 2013 and continues to date. Approximately ≃840 horizontal hydraulic fracturing well completions have been performed up to December 2020 in the Duvernay Fm., SSO No. 2 area. To investigate the migration patterns in the injection volume intensity from hydraulic fracturing activities, we elaborated a series of maps that shows the spatial distribution of the cumulative hydraulic fracturing volumes (m^3) injected into the Duvernay Fm. These maps are built by adding all volumes in discretized areas of approximately ≈180 km^2. The total volume is plotted at the center of the discretized areas and then interpolated to generate contour maps.

To discriminate between seismogenic and non-seismogenic wells, first, we refine the earthquake location using double-difference relocations with the HypoDD algorithm (Waldhauser, 2001; Waldhauser & Ellsworth, 2000).

Then, we perform a Spatiotemporal Association Filter as implemented by Schultz et al. (2018) to analyze the induced seismicity in Fox Creek. The first condition specifies that earthquakes may not occur before the first stage completion at a pad and may occur up to 3 months after completion of the final stage. The second condition establishes that the epicenters of all temporally associated earthquakes are within 5 km of the well pad surface location (Schultz et al., 2018).

To describe the non-stationary behavior of the induced seismicity in Fox Creek, we split the earthquake catalog per year and then estimate the magnitude of completeness (M_c) for each year using Maximum Curvature Methods (MCM, Wiemer & Wyss, 1997). The magnitude of completeness (M_c) in the Fox Creek area shows values of $M_c > 3$ prior to 2013, with a rapid decrease to $M_c \simeq 2$ in 2014 as a consequence of the deployment of seismological stations in the area (Regional Alberta Observatory for Earthquake Studies Network, Schultz & Stern, 2015). The completeness magnitudes kept decreasing, reaching a $M_c \simeq 1.7$ by 2018, and $M_c \simeq 1.4$ by 2020. Once the M_c has been calculated per year, we proceed to estimate the annual GR parameters, $a(t)$- and $b(t)$-values, using Maximum Likelihood Methods (MLM, Aki, 1965; Wiemer & Wyss, 1997), and considering the magnitude binning of the catalog. For the estimations of the b-value error, we use the method described by Shi and Bolt (1982), which provides an upper and lower bound for the b-value. Knowing the bounds for the $b(t)$-value (upper and lower $b(t)$-values) and the number of events larger than a given magnitude in the catalog (e.g., M_c), the GR recurrence law (Equation 1) is then invoked to estimate the upper and lower bounds for the $a(t)$-value (upper and lower $a(t)$-values). Once the annual GR parameters, $a(t)$- and $b(t)$-values, have been calculated, we proceed to calculate the annual rate of exceedance $\lambda_{\text{exc}}(m \geq m_j, t)$ for magnitudes greater than $M > 4$ (Equation 3). Then, by assuming a Poisson distribution (Equation 9), we estimate the likelihood of n earthquakes with a magnitude greater than $M > 4$ per year, from $a(t)$- and $b(t)$-values derived from MLM, and their upper and lower uncertainty boundaries. Other metrics of hazard can be used, for instance, the likelihood of n earthquakes with a magnitude greater than $M > 3$ per year (see Supporting Information). However, we give special attention to the events larger than $M > 4$ since this is the magnitude threshold for the red-light earthquakes according to the traffic light protocol in the SSO No. 2 area.

The use of Equation 9 for seismic hazard forecasts is permitted even if the earthquake distributions are different from a Poissonian process, for instance, due to the existence of aftershock sequences, as shown by Reyes Canales and van der Baan (2020). Additionally, some studies, including Hajati et al. (2015) and Langenbruch et al. (2011), have shown that the non-stationary Poisson process can be assumed as a very good approximation to model fluid-induced seismicity.

To better understand the causes that lead to the reduction in the seismic hazard in the Fox Creek area, we analyze the Western and Eastern regions of the seismic cluster independently (see Figure 1a). We observe that both the Western and Eastern sections show different seismic features, with the Eastern section containing most of the events larger than $M > 3$, and all the events larger than $M > 4$. We proceed to calculate annual annual GR parameters, $a(t)$- and $b(t)$-values, and the likelihood of n earthquakes with a magnitude greater than $M > 4$ per year, to conduct a seismic hazard study for the Eastern and Western regions individually and the entire area.

4. Fox Creek Induced Seismicity Case: Changes in the Hydraulic Fracturing Activities and Annual Likelihood of Moderate Events

4.1. Evolution of the Seismicity and Hydraulic Fracturing Operational Parameters

The number of earthquakes in the Fox Creek area increased dramatically after December 2013, in line with the emergence of seismogenic wells related to hydraulic fracturing activities in the Duvernay Fm. Figure 1b shows the annual number of hydraulic fracturing wells in the Duvernay Formation, SSO No. 2 area (blue bars), and the number of positively correlated seismogenic wells (magenta bars) per year. Notice that the annual number of hydraulic fracturing wells remains relatively similar from 2015 until 2019, reaching a maximum in 2018. On the other hand, the number of positively correlated hydraulic fracturing wells remains stable between 2015 and 2018 and then drops in 2019 and 2020. A noticeable decline in the number of wells and injected volumes occurred in 2020, likely related to adverse economic conditions and the COVID-19 pandemic. The black curve in Figure 1c shows the annual hydrocarbon production (in BOE) from the Duvernay Fm., SSO No. 2 area. The hydrocarbon production in the Duvernay Fm. has consistently increased, peaking in 2020, in contrast with decreasing seismicity, particularly events with magnitude larger than $M > 3$.

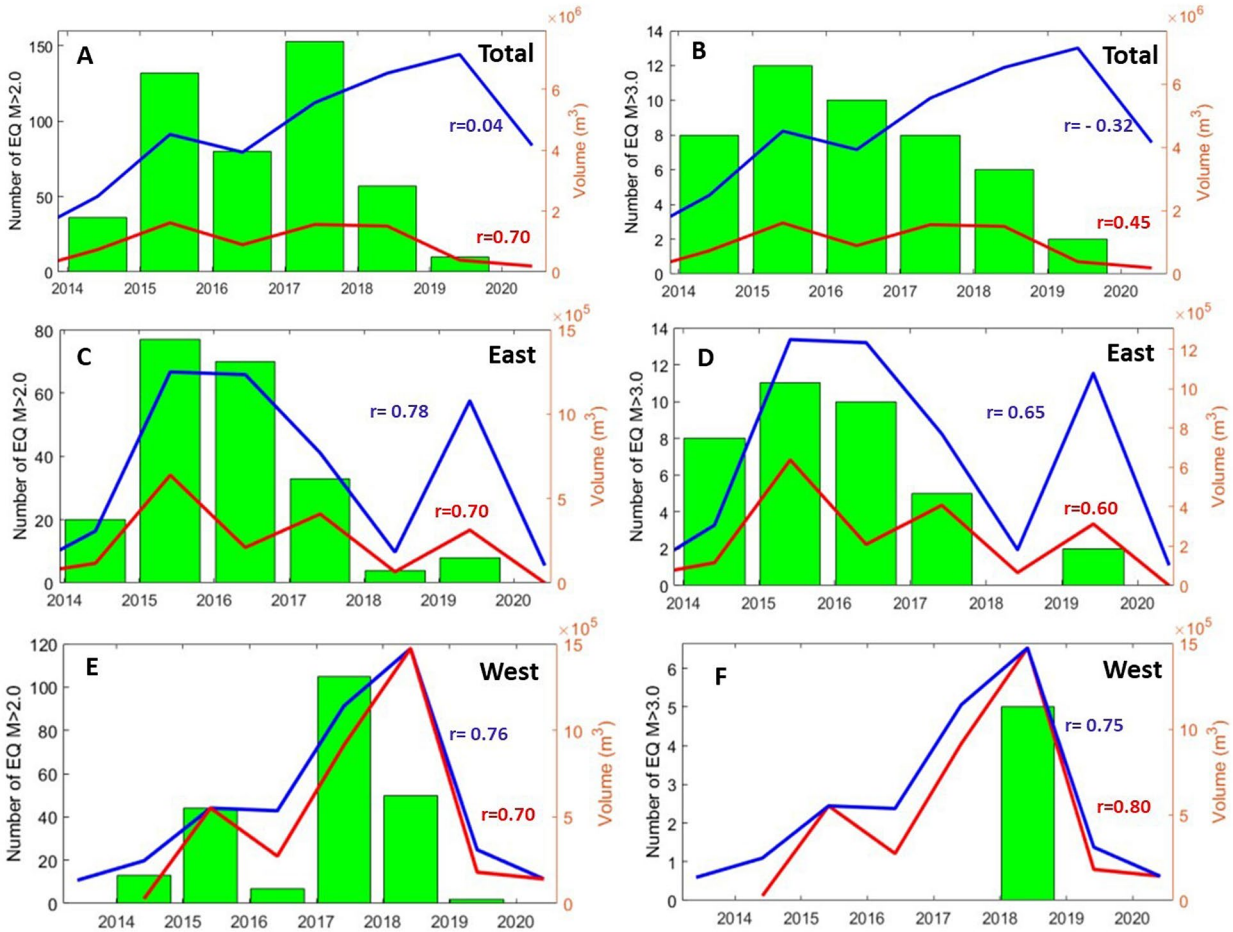

Figure 2. Annual number of earthquakes larger than magnitude $M > 2$ (a, c, and e green bars) and, $M > 3$ (b, d, and f green bars). Total hydraulic fracturing volumes injected per year, from all wells (blue line) and seismogenic wells (red line), for the entire SSO2 area (upper row), and the Eastern and Western sections of the seismic cluster (medium and lower row). The correlation coefficient (r) between the seismicity and the hydraulic fracturing volumes (blue for all wells, red for seismogenic wells) are included in the figure.

Figures 2a and 2b show the total hydraulic fracturing volumes injected per year in the Duvernay Fm., SSO No. 2 area, from all wells (blue curve) and seismogenic wells (red curve). These figures also contain the annual number of events larger than $M > 2$ (A) and $M > 3$ (B; green bars). The peak in the overall number of earthquakes larger than $M > 2$ was reached in 2017, with more than 150 earthquakes recorded that year (See Figures 2a and 2b). The number of earthquakes larger than $M > 3$ peaked in 2015, with 12 events. Since then, the number of earthquakes $M > 3$ has declined, reaching 2 events in 2019, and no events $M > 2$ in 2020. As explained before, we use the criteria defined by Schultz et al. (2018) to correlate the hydraulic fracturing wells with the relocated seismicity and identify the seismogenic wells. Only hydraulic fracturing wells with neighboring seismicity (5 km or less) that occur in a specific time window (from the start of the pad operations to three months after concluding the pad operations) are positively correlated and considered seismogenic wells. We found that approximately $\simeq$15% of the wells are seismogenic. From Figures 2a and 2b, the total hydraulic fracturing volumes steadily increased per year, except for a drop in 2016 and 2020. It should be noticed that the peak in the number of earthquakes $M > 2$ (2017) contrasts with the peak in the number of earthquakes $M > 3$ (2015), and the peak in the overall injection volumes from hydraulic fracturing wells (2019). Also, for the seismogenic wells, the volumes remain relatively similar after 2015, with a drop in 2016, and then in 2019 and 2020.

Seismicity is mostly located west of Fox Creek (Figure 1a) in a Western and Eastern cluster. Hydraulic fracturing activity within these two clusters shifts over time. Figures 2c and 2d show the annual hydraulic fracturing volumes for the Eastern cluster and the annual number of events larger than $M > 2$ (A) and $M > 3$, respectively. Likewise, Figures 2e and 2f show the same information for the Western cluster. Hydraulic fracturing peaked in

2015 and 2016 in the Eastern portion, moved in 2017 and 2018 to the West, only to return in 2019 to the Eastern portion. All activity declined sharply in 2020 due to the COVID-19 pandemic and its economic impact. The proportion of seismogenic wells in the Eastern and Western clusters are also different, with 40% of the wells in the Eastern cluster associated with seismicity versus 70% of the wells for the Western cluster. The number of events larger than $M > 2$ (A) and $M > 3$ in the Eastern cluster correlates well, except for 2014, where 40% of recorded events comprise an $M > 3$ event (Figures 2c and 2d). The latter correlation may be due to a magnitude of completeness larger than 2 for this year. Conversely, for the Western cluster (Figures 2e and 2f), no events $M > 3$ occur except in 2018. Seismicity, however, peaks in 2017 in this area, with over 100 events.

Figure 2 includes the correlation coefficient between the seismicity and the volumes from hydraulic fracturing wells (all wells and seismogenic wells) in the SSO2 area and the Eastern and Western regions. We observed a good correlation between volumes and seismicity for the Eastern and Western clusters, with higher correlation coefficients between the events $M > 2$ and the volumes from both Eastern and Western regions, and a lower correlation coefficient between events $M > 3$ and the volumes from the Eastern region. In contrast, the correlations coefficients for the SSO2 area show a weak, even a negative correlation between seismicity and volumes from all hydraulic fracturing wells.

4.2. Annual Likelihood of Events Larger Than $M > 4$

We calculate the annual GR parameters for the total seismic cluster, as well as the Eastern and Western regions, using the observed earthquake catalog recorded in the Fox Creek area (AGS earthquake catalog). For the estimation of b-values, we relied on annual earthquake catalogs and implemented MLM, and for the Magnitude of completeness, we implemented MCM (See Figures S1 to S3 in the Supporting Information S1 for the annual Magnitude-frequency distributions and GR parameters). From the annual GR parameters and by assuming a Poisson process, we calculate the likelihood of n earthquakes with a magnitude greater than $M > 4$ per year, using a maximum magnitude of $M_{\text{Max}} = 6.5$, which is based on the largest magnitude assumed in the preliminary seismic hazard evaluation conducted by Atkinson et al. (2015) in this area. We analyze the likelihood of earthquakes with magnitude $M > 4$, since this is the magnitude threshold for red-light events in the area (Alberta Energy Regulator, 2015). As a consequence, we set a minimum magnitude $M_{\text{Min}} = 4.0$ in Equations 3 and 5.

The left column in Figure 3 shows the evolution of annual a- and b-values in the Fox Creek area, given the full cluster, as well as the Eastern and Western sections. Notice that, for the full cluster, two phases have been identified: Phase 1 (2014–2016) with b-values below $b < 1$, and Phase 2 (2017–2020) with b-values above $b > 1$. These phases represent the evolution of the seismic hazard in the Fox Creek area. Phase 1 and 2 are respectively dominated by seismicity in the Eastern and Western clusters (Figures 2c and 2f), although some renewed seismicity in the Eastern cluster occurs in 2019.

There is a significant difference in the b-values between the Eastern and Western sections, both displaying relatively minor changes over time. The b-values for the Eastern section range between $b = 0.67$ (2014) and $b = 0.99$ (2019), whereas the Western section shows larger b-values ranging between $b = 1.43$ (2018) and $b = 2.49$ (2020). The b-values for the Eastern section during 2018 and 2020 are not considered in the analysis due to the low seismicity in those periods.

The right column in Figure 3c shows the annual likelihood of events with a magnitude larger than $M > 4$, for the full cluster and its Eastern and Western sections. For simplicity, we assume that the annual GR parameters remain constant for each year and that the seismicity occurs randomly in time following a Poisson distribution (Equation 9). The blue curve shows the likelihood predicted by the GR parameters estimated using MLM. The red and green curves show the upper and lower seismic hazard scenarios, based on the uncertainty in the GR parameters. From the analysis of the full cluster, the likelihood of events larger than $M > 4$ peaked in 2015, with a 95% probability. Since then, the likelihood has decreased consistently to 60% in 2016, 18% in 2017, 10% in 2018 4% in 2019, and less than 1% probability in 2020. For reference, 3 earthquakes $M > 4$ were recorded in 2015, and 1 earthquake $M > 4$ in 2016. Notice that the peak in the overall seismicity occurred in 2017. However, due to a substantial increase in the b-values, the likelihood of large earthquakes decreased to 18%. Furthermore, no earthquakes with a magnitude $M > 4$ have been recorded since 2016 in the Fox Creek area.

Figure 3 also demonstrates that the Eastern section has largely dominated the seismic hazard in Fox Creek, except for the years 2018 and 2020. The likelihood of events larger than $M > 4$ peaked in 2015 for the Eastern section,

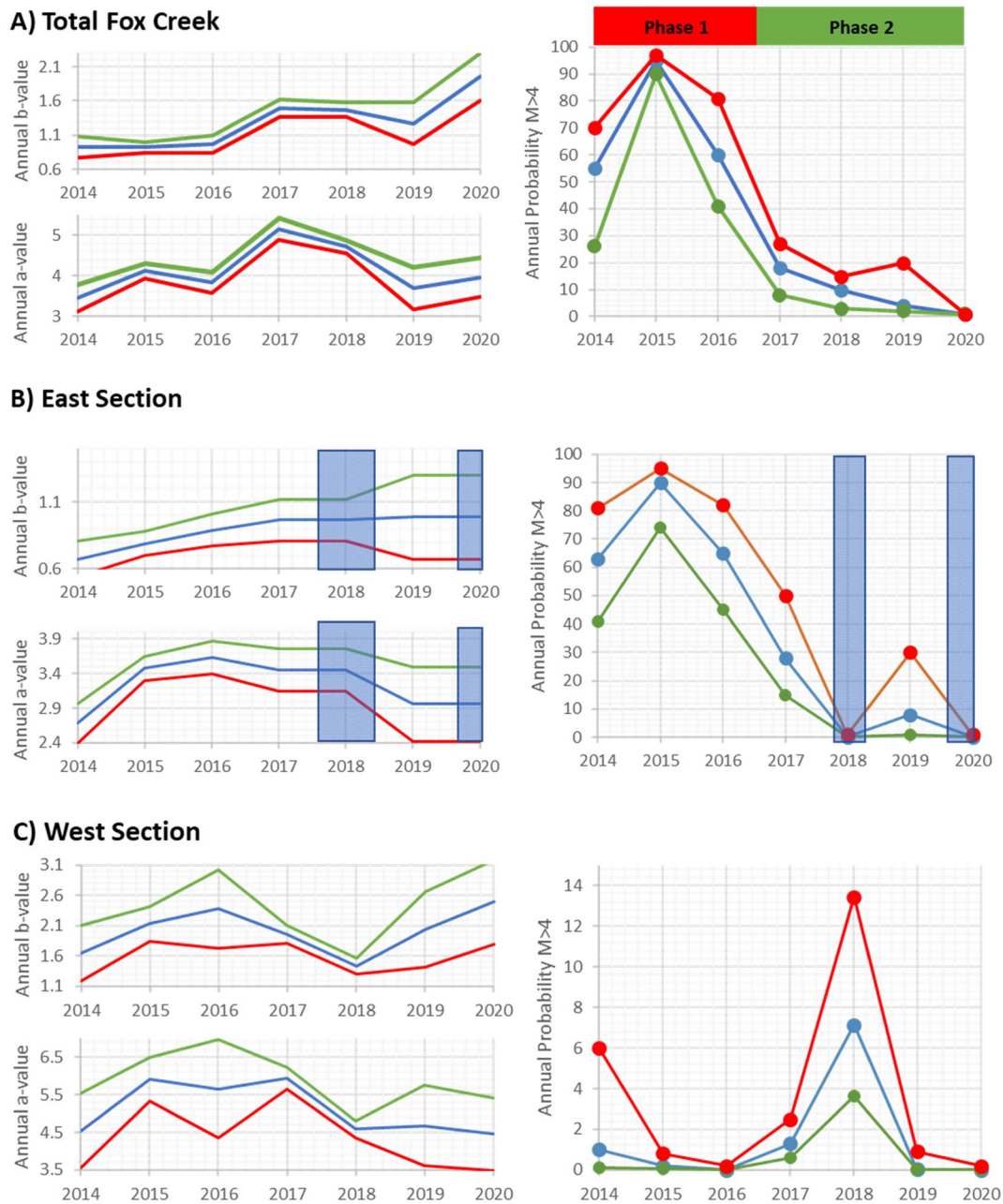

Figure 3. The left column shows the temporal evolution of the annual b and a-values for the full seismic cluster (a), as well as the Eastern (b) and Western (c) subclusters. The right column shows the annual probability of earthquakes larger than $M > 4$ for the full seismic cluster (a), as well as its Eastern (b) and Western (c) portions. The blue curves shows the hazard scenarios (middle case) derived from the estimated GR parameters. The green and red curves show the lower- and upper-case hazard scenarios incorporating parameter uncertainties. The results of the Eastern section for 2018 and 2020 are masked (shaded blue) due to the limited seismicity in those years.

with a 90% probability. Since then, the likelihood has decreased considerably, including periods of very low seismicity (2018 and 2020) due to a sharp decline in hydraulic fracturing activity (Figures 2c and 2d). The initial high hazard is caused by the low b-values and the relatively large number of events (a-values) in this subcluster, which decline after 2016. The reactivation in 2019, showing again relatively low b-values, is compensated by a rapid decrease in a-values, resulting in an overall reduction of the seismic hazard for that year.

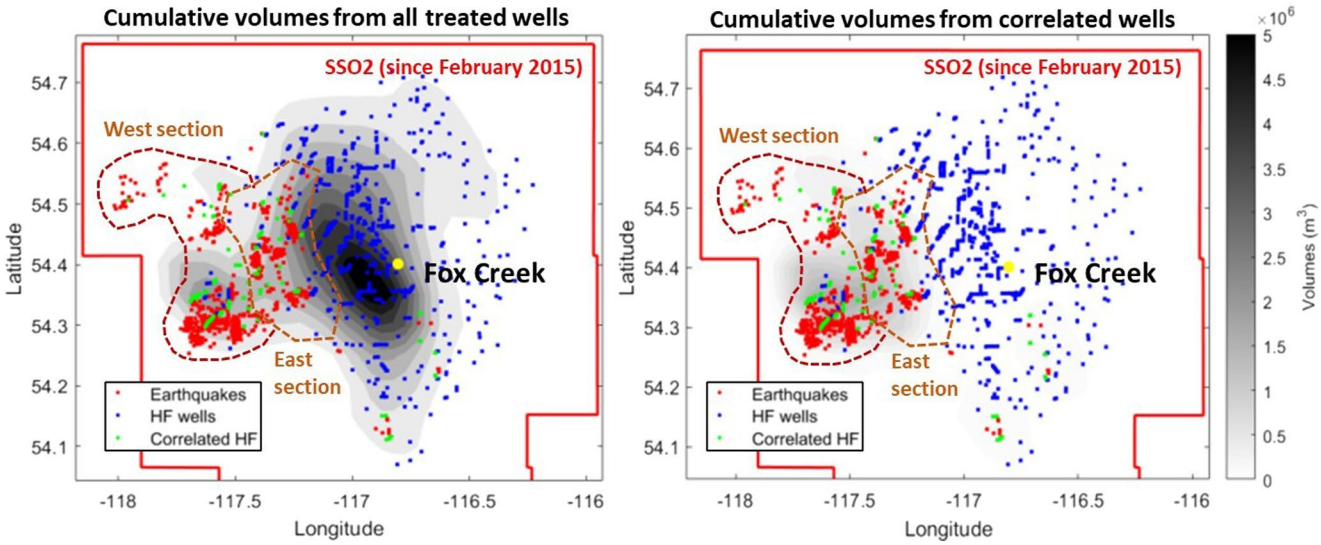

Figure 4. Hydraulic fracturing volumes (in m^3, greyscale) injected into the Duvernay Fm. and earthquakes in the Fox Creek area. between 2010 and 2020. (a) Cumulative volumes from all hydraulic fracturing wells in the Duvernay Fm., and (b) cumulative volumes from positively correlated seismogenic wells. Red dots: relocated events from the earthquake catalog between 2013 and 2020. Blue dots: location of the hydraulic fracturing wells. Green dots: hydraulic fracturing wells positively correlated with the seismicity.

On the other hand, for the Western section, the likelihood of events larger than $M > 4$ peaked in 2018, with a 7% probability (Figure 3c), when operator activity shifted from the Eastern to the Western section (Figure 2). Furthermore, at its peak in 2017, 105 events $M > 2$ occurred in the Western portion versus 70 (2016) and 77 (2015) in the Eastern portion. The Western portion is clearly quite seismogenic, yet with a lower likelihood for inducing moderate-sized events of $M > 4$. The difference in seismic hazard is, in this case, primarily caused by strongly different b-values for the two areas, with average b-values of $b = 0.86$ and $b = 2.01$ for the Eastern and Western portions, respectively. This difference is again demonstrated when the seismogenic hydraulic fracturing activity moves back to the East in 2019 (Figures 2c and 2d), yet accompanied by solely a modest increase in seismic hazard (Figures 3a and 3b), since the hazard is substantially reduced compared to previous levels (2014–2016) despite similar injection volumes (Figures 2c and 2d).

Our analysis illustrates that seismic hazard due to hydraulic fracturing is not necessarily dominated by regions with the highest association statistics between treated wells and nearby seismicity but by areas displaying the lowest b-values, combined with a sufficient number of events. Therefore, it is important to look for subclusters within the spatial distribution of epicenters (Figure 1) to get a clear understanding of underlying causes and trends. Such analysis hinges on the completeness of any catalogs and the availability of sufficient observed seismicity to compute magnitude-frequency distributions and their characteristics reliably.

4.3. Migration of the Injection Volume Intensity From Hydraulic Fracturing Activities in the Duvernay Fm

To investigate these trends further, we generate a series of maps that shows the spatial distribution of the cumulative hydraulic fracturing volumes (m^3) injected into the Duvernay Fm. and the location of induced earthquakes (Figure 4). The injection volumes per relevant well have been added in discretized areas of approximately $\approx$180 km^2. The total cumulative volume is plotted at the center of the discretized areas and then interpolated to generate the contour maps. The red dots show the relocated induced earthquakes, the black dots the location of the hydraulic fracturing wells, and the green dots the location of the seismogenic wells.

Figure 4a shows the total cumulative volumes (m^3) per discretized area injected into the Duvernay Fm., between 2010 and 2020, from all hydraulic fracturing wells. Notice that the highest cumulative volumes occur East of the main cluster of relocated earthquakes, showing a mismatch between areas with higher injection volumes and earthquake occurrence. Figure 4b shows the cumulative volumes from only positively correlated hydraulic fracturing

wells. In this case, the location of the full cluster of earthquakes approximately correlates to the areas with higher volume injection, with the exception of the northwest tip of the Western cluster, where seismicity occurs at low injection volumes. Also, the seismicity in the southwest tip of the Western cluster is slightly placed to the South of the main injection area. As observed in previous studies, like Schultz et al. (2018), the correlation between the number of earthquakes and injection volumes is evident only when the well is seismogenic. In other words, this result shows that the areas with higher injection volumes do not necessarily show relevant seismicity, but the appropriate geological conditions are required for the occurrence of induced earthquakes (Van der Baan & Calixto, 2017).

Because the location of industrial activity changes over time, we generate annual maps showing the variations in the spatial distribution of the cumulative hydraulic fracturing volumes injected into the Duvernay Fm (Figure 5). Notice that prior to 2013, the volume intensity and the number of wells were relatively low since this period coincides with the start of operators exploring the economic potential of the Duvernay Fm. Induced seismicity started in December 2013 within the Eastern subcluster in an area with a relatively low cumulative injection. In 2014 most of the volumes are injected west of Fox Creek, with the induced earthquakes located in areas with, again, lower injected volumes toward the North-West but now within the Western subcluster. For 2015 and 2016, two areas with high injection volumes are observed, located respectively entirely inside the Western subcluster and partially within the Eastern subcluster with associated induced seismicity. In 2017, operators target two areas with high injection volumes, one north of Fox Creek, outside the Eastern subcluster with absent seismicity, and a second area within the Western subcluster with incidents of induced events. Seismicity occurs, however, in areas of moderate injection volumes. For 2018 we observe three areas with high injection volumes, two of them located north and south of Fox Creek, respectively, outside of the Easter subcluster and with absent induced seismicity. The third one straddles the border of the Western and Eastern sections. Yet seismicity occurs nearly entirely within the Western subcluster, again predominantly in areas with low-to-moderate injection volumes such as its northwest tip. By 2019, the areas with the highest injection volumes are located South of Fox Creek, primarily outside of the Eastern subcluster, with induced events in areas with comparatively lower injection volumes in both the Eastern and Western sections. Finally, a similar trend is observed in 2020, where the areas with higher injection volumes are located South of Fox Creek without induced events. Some events occurred in the Western section. Seismicity is almost absent in the Eastern section.

Figure 5 shows a more nuanced evolution in injection volumes and induced seismicity than Figure 4. However, a common trend derived from these maps is that the seismic events generally occur west of Fox Creek in areas of small-to-moderate injection volumes, whereas the hydraulic injection intensity has migrated to other areas north and south of Fox Creek, particularly after 2016. This agrees with previous observations (Eaton & Schultz, 2018; Pawley et al., 2018) that describe the area west of Fox Creek as susceptible to induced events. The evolution of the injection volumes in Figure 5 agrees with the annual trends described in Figure 3. For the West section, increasing volumes appear in the maps in 2015, reaching a peak of intensity in 2018, and declining afterward. A similar trend is observed in the annual plots from Figure 3. The injection volumes in the East section intensify in 2014, peaking in the period 2015–2016, and followed by declining activity with a second period of increasing volumes in 2019. Finally, some of the areas with high volume injection toward the East tend to move away from the Western and Eastern clusters, particularly since 2017, which agrees with the trend of increasing volume in the SSO2 area, but a reduction of seismicity is observed in Figure 3.

5. Discussion

5.1. Reduced Likelihood of Moderate Events in the Duvernay Fm., Fox Creek Area

The statistical analysis in this study suggests that the likelihood of earthquakes larger than $M > 4$, and associated seismic hazard, has consistently declined after its peak in 2015 in the Fox Creek induced seismicity case, in contrast with increasing hydraulic fracturing activities. There are multiple factors that can help explain these observations:

1. One of the critical factors is the intensification of hydraulic fracturing activities in the Duvernay Fm. toward areas less susceptible to induced seismicity. The migration of the highest volume injection toward the East and out of the seismogenic area, particularly after 2016, also explains the hazard reduction despite the overall hydraulic fracturing activities increasing until 2019. For instance, in some years like 2019, the most intense

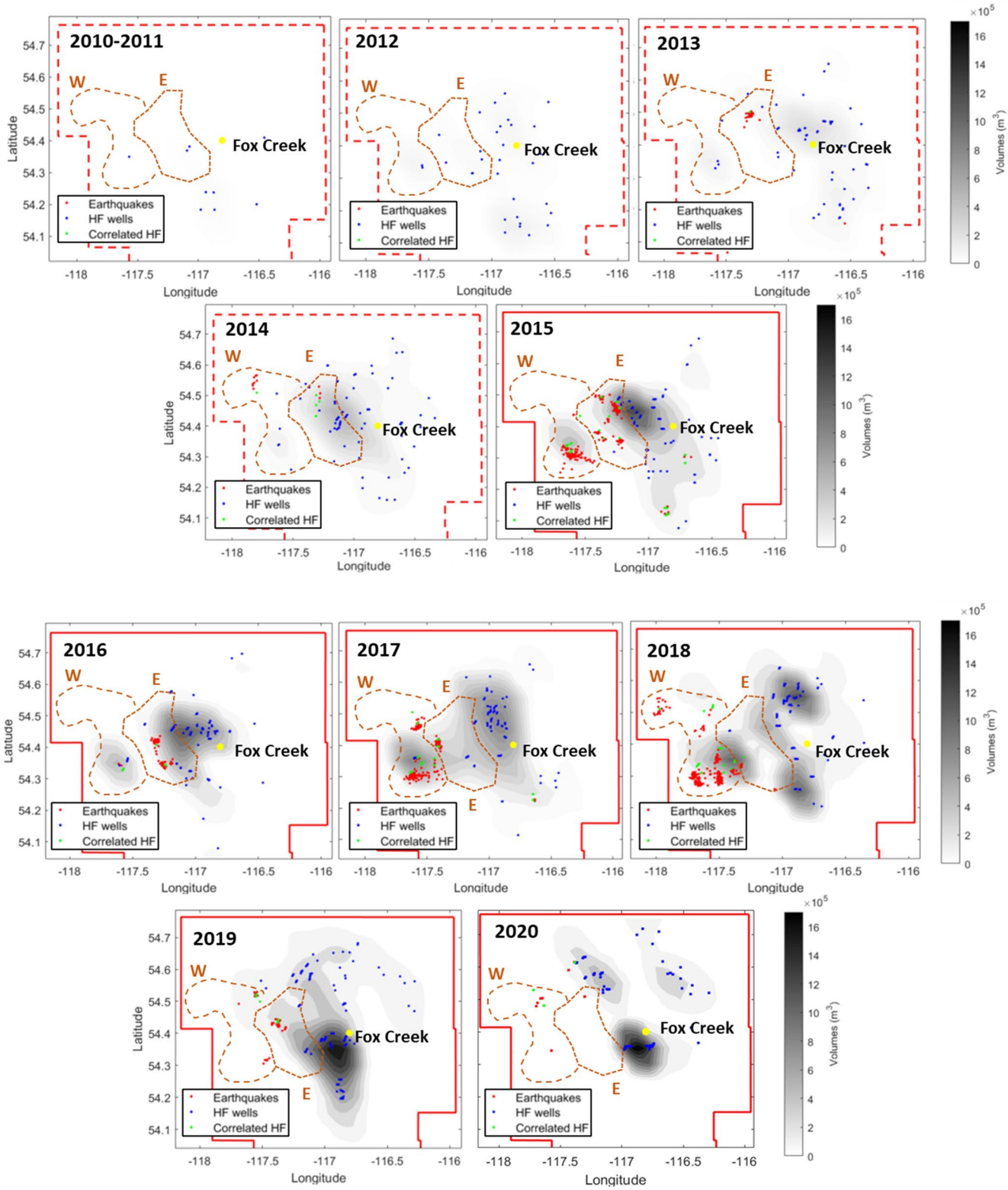

Figure 5. Hydraulic fracturing volumes injected into the Duvernay Fm., per year and relocated earthquakes in the Fox Creek area. The background color shows the annual cumulative hydraulic fracturing volumes (m^3) per discretized area injected into the Duvernay Fm. from 2010 until 2020. The years 2010 and 2011 are combined due to the relatively low hydraulic fracturing operation intensity. Labels, symbols and legends as in Figure 4.

treatment activity by volume occurred outside of the most susceptible induced-seismicity areas in the West, that is, outside of the Eastern and Western subclusters.

2. Another key factor is the substantial reduction in induced seismicity in the Eastern sub-cluster. This area has largely dominated the seismic hazard in Fox Creek, except for the years 2018 and 2020. The reduction in the seismic activity can be partially explained by the overall reduction in the hydraulic fracturing volumes after 2015. However, the volumes from the seismogenic wells remain substantial, particularly during the rises in 2017 and 2019, suggesting that changes in the hydraulic fracturing strategies have played a role in reducing the seismic hazard.
3. A reduction in seismic hazard is likely influenced by mitigation efforts of operators in response to growing awareness and regulatory action. In February 2015, the Alberta Energy Regulator introduced a traffic light protocol as a part of the new monitoring and reporting requirements (SSO No. 2, Alberta Energy Regulator, 2015). Therefore, all Duvernay operators in the Fox Creek area must report all adjacent events $M > 2.0$ (yellow-light event) and implement mitigation strategies. Furthermore, if an event $M > 4$ occurs (red-light event), the operations must cease immediately. The 2015 regulations and changes in treatment strategies implemented by the operators have been pertinent factors in reducing the likelihood of $M > 4$ events and associated seismic hazard.

The mitigation strategies implemented by the operators can vary and may include pausing and/or stopping the operations during a pertinent time to reduce the reservoir stress, skipping stages in formation intervals of concern, decreasing the fluid injection rate and volumes, altering the treatment fluid content, or moving from multi-well zipper to single-well completions (Ground Water Protection Council and Interstate Oil and Gas Compact Commission, 2021). Furthermore, pre-seismic hazard assessments are common in areas susceptible to induced seismicity, like Fox Creek. In these assessments, potential seismogenic faults are identified, and the hydraulic fracturing plans are designed to minimize the pore pressure perturbation in these potential seismogenic faults. In this scenario, operators might skip some stages, pause the operations, change the injection fluids, and/or reduce the injection volume/rates/pressures of the hydraulic fracturing stimulation to minimize the pore-pressure perturbation near the fault (Schultz et al., 2020). In many cases, the identification of seismogenic faults is not straightforward, and they are not discovered until the hydraulic fracturing stimulation phase. Challenges are in particular imposed by strike-slip faults, which are difficult to identify on reflection seismic data since there is little to no offset visible in the formations across the fault (Eaton et al., 2018). Reactivation of strike-slip faults is the dominant source mechanism for moderate-sized events in the Fox Creek area (Schultz et al., 2017; Wang et al., 2017).

Another valuable tool during the mitigation phase is the near-real-time detection and relocation of earthquakes, allowing operators to map lineaments within critical stressed orientation. Special attention is required to those reactivated basement-rooted faults with a favorable orientation to slip since this is the most common style of fault observed to cause induced seismicity in the Fox Creek area (Eyre et al., 2019). Statistical changes in recorded seismicity can also give insights from potential fault activation and the likelihood of moderate events. For instance, sudden drops in the *b*-values could indicate the upcoming occurrence of mainshocks (Gulia & Wiemer, 2019); therefore, this can be a warning sign to modify the operational parameters and manage the seismic hazard. Similar observations have been made by van der Elst (2021) with a new estimator named "*b*-positive', which can be used to forecast upcoming mainshocks and circumvent possible biases that appear in the temporal variations of *b*-values with unknown or variable completeness. As an extension of these statistical analyses, physics-based models like the seismogenic index (Langenbruch & Zoback, 2016; Shapiro et al., 2010), as well as the hydromechanical nucleation approach (Norbeck & Rubinstein, 2018), can be used to forecast the number of earthquakes from upcoming operations. However, care should be taken that these approaches assume constant *b*-values, thereby only forecasting event rates above a certain magnitude, thus providing only limited information on the seismic hazard (Reyes Canales & van der Baan, 2021). Nonetheless, such forecasting approaches can provide insight into likely future trends given operational scenarios, once calibrated against historical data.

To test if the operators have improved their management of induced seismicity, we study the temporal evolution of the Seismogenic Index and the threshold volumes in the Eastern and Western sections of the seismic cluster. The Seismogenic Index describes the volume concentration of preexisting faults and the state of stress in one particular area (Langenbruch & Zoback, 2016; Schultz et al., 2018; Shapiro et al., 2010). The Seismogenic Index modifies the GR relationship to allow time-dependent *a*-values. In this model, the *a*-values increase depending on the volume injected and the Seismogenic Index, thus relating the seismic response to increasing fluid injection.

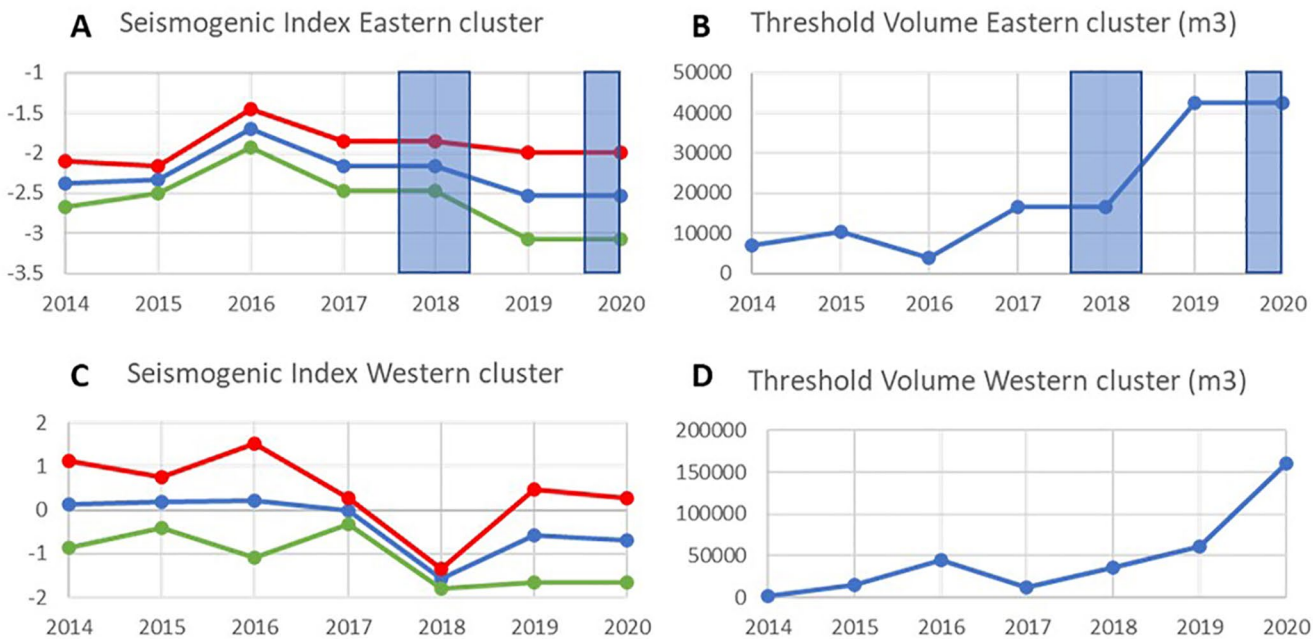

Figure 6. The left column shows the temporal evolution of the Seismogenic Index for the Eastern (a) and Western (c) clusters. The right column shows annual threshold volume for the Eastern (b) and Western (d) clusters. The results of the Eastern section for 2018 and 2020 are masked (shaded blue) due to the limited seismicity in those years. Note different vertical scales between rows.

For the calculation, we use the annual *a*-values and only injection volumes from seismogenic wells in both Eastern and Western sections. On the other hand, the threshold volume refers to the minimum injection volume required to generate events larger than a given magnitude (Langenbruch & Zoback, 2016; Schultz et al., 2018). We implement the methodology described by Schultz et al. (2018) for the estimation of the threshold volumes, and we set the analysis to calculate the minimum injection volume required to activate events larger than magnitude $M > 2$. For more details about the Seismogenic Index and the threshold volumes, the reader is referred to the Supporting Information.

Figures 6a and 6c show the temporal evolution of the annual Seismogenic Index in the Eastern and Western sections. In theory, the Seismogenic Index in a region should remain constant over time unless the concentration of preferably oriented faults and/or the state of stress changes; however, past observations indicate this parameter may be time-dependent in areas with active hydraulic fracturing treatments (Reyes Canales & van der Baan, 2021). From Figure 6, we observe that the Seismogenic Index for the Western section is substantially higher than the Seismogenic Index from the Eastern cluster; in other words, a smaller volume in the Western cluster leads to more seismicity (higher earthquake rates). However, this is not necessarily translated to larger magnitude events due to the large *b*-values in the Western region.

Figures 6b and 6d shows the annual changes in the threshold volumes for the Eastern and Western sections. From these figures, the threshold volume increases over time for both clusters. We outline two potential causes, either as a consequence of changes in location or a change in the treatment strategies. In the case of changing locations, the operations (by design or fortuitously) are further away from any seismogenic faults; thus, larger volumes are required to produce sufficient stress perturbations in distant faults and trigger seismicity. In the interpretation of changed treatment strategies, operators have improved their handle on induced seismicity and can, therefore, increase the injection volumes avoiding activation of large fault segments and thereby larger events. From Figures 6b and 6d, we observe that the threshold volume of the Western cluster is either comparable or up to twice as large as the threshold volume for the Eastern cluster up to 2019. The threshold volume significantly diverges in 2020 for the Western cluster. The relatively high threshold volumes for the Western cluster imply that more volume is required in order to have associated seismicity. The divergence in 2020 could be again due to spatial locations and/or treatment strategies.

Two causes may explain the declining values of the Seismogenic Index for both sections since 2016, which might imply a change in spatial locations or treatment strategies. The decrease in the seismogenic index could be a consequence of operators actively avoiding regions with higher seismogenic indices, yet there is no indication of active avoidance strategies at the scale of Figure 5. Another option is that operators have improved their handle on induced seismicity and can increase the injection volumes while triggering solely smaller or no events, for instance, due to improved mitigation strategies facilitated by enhanced monitoring and increasing regulatory scrutiny in case of yellow traffic light events. Therefore, larger volumes are required over time to breach the injection threshold, in return changing the Seismogenic Index.

Revisiting Figures 4 and 5, we can infer that the operators change their injection volumes depending on the induced seismicity generated, particularly for events $M > 3$. This may explain why the Eastern cluster has somewhat lower injection volumes than the Western cluster (except for the northwest tip of the Western cluster). This would imply that increased monitoring due to imposed regulations is effective, combined with induced seismicity concern from operators. The operators are clearly using larger volumes in the non-seismic areas east of the cluster. However, these changes in volume may also be related to lateral changes in reservoir conditions.

In general, and due to large *b*-values, the Western section has shown a considerably lower likelihood of moderate events than the Eastern section. The observed variations in the *b*-values from the total cluster (Figure 3a) result from an interplay between the activation of both regions: an initial phase 1 (*b*-values < 1, between 2014 and 2016) largely dominated by an over-active Eastern section and a less active Westen section, and a phase 2 (*b*-values > 1, between 2017 and 2020) with a drastic reduction of activity in the Eastern section, and a Western section gaining comparatively more importance. It should be noted that, by calculating the likelihood of moderate events from the entire catalog, we obtain comparable results to those estimated by studying the Eastern and Western sections separately. However, as mentioned earlier, it is recommended to study each small cluster independently when possible. Unfortunately, one of the challenges with increasing the spatial and temporal discretization of an earthquake catalog is the reduction in the number of earthquakes, which ultimately compromises the calculation of the recurrence parameters.

5.2. Reservoir and Stress Properties of the Duvernay Fm. in Areas Susceptible to Hydraulic Fracturing Induced Seismicity

Multiple geological proxies have been proposed for the induced seismicity in the Fox Creek area. For instance, Pawley et al. (2018) suggest increased induced seismicity susceptibility in the Duvernay Fm. when the pressure-to-depth ratio increases and the distance from the operations to the basement decreases. High pore pressure lowers the effective normal stress on a fault, reducing the resistance to frictional sliding. Thus, overpressured conditions facilitate the generation of seismic events in susceptible faults under the stress perturbation caused by the hydraulic fracturing simulations (Eaton & Schultz, 2018; Ries et al., 2020). In the case of the proximity to the basement, basement rooted faults may be larger than the sedimentary layers above, as well as more continuous, increasing the likelihood of larger events (Kozłowska et al., 2018).

The analysis conducted by Eaton and Schultz (2018) also suggests that the likelihood of induced seismicity increases in highly overpressured shale formations, like the Duvernay Fm. west of Fox Creek. To corroborate these observations, we plot pressure gradient models in the Duvernay Fm. with the location of the induced events (Figure 6). The simulated pressure gradient (kPa/m) for the Duvernay Fm. is based on the analysis conducted by Lyster et al. (2017), who characterize some of the main geological properties of the Duvernay Fm. to evaluate its hydrocarbon resource potential. In Figure 6, notice the good agreement between the induced earthquakes, seismogenic wells, and the overpressured areas in the Duvernay Fm. However, the use of pressure gradients as a general proxy for induced seismicity should be taken cautiously since this correlation might not be clearly observed in other shale plays prone to induced seismicity. For instance, in the susceptibility analysis conducted by Wozniakowska and Eaton (2020) for the Montney Fm., the relevance of the pressure gradient as a proxy for induced seismicity was reduced in favor of other factors, particularly the distance to the cordillera belt, injection depth and distance to the basement. It is possible that some of these factors correlate to changes in the tectonic stresses, a causative factor that is explicitly ignored when solely considering pore pressure variations (Hager et al., 2021; van der Baan, 2021).

To understand the possible causes why the Eastern and Western subclusters are more susceptible to induced seismicity than other nearby areas, we collect and analyze stress and reservoir properties from areas that are seismogenic and non-seismogenic, using the Duvernay studies of Lyster et al. (2017) and Shen et al. (2018). For

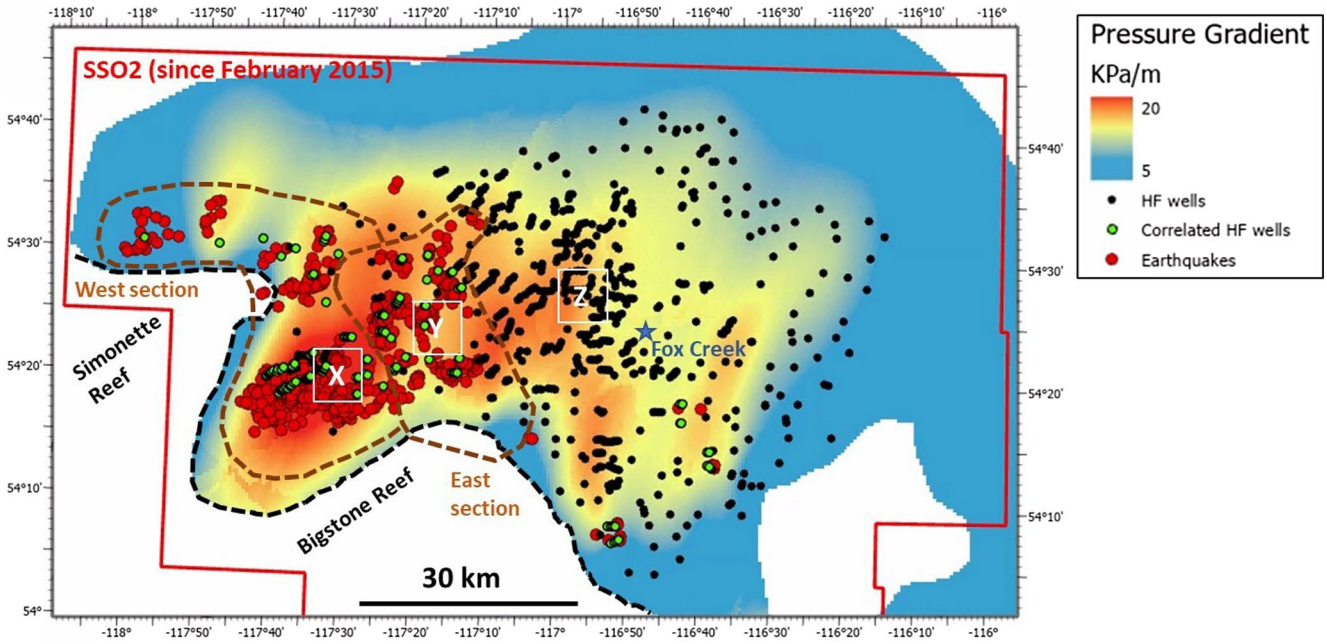

Figure 7. Simulated pressure gradient in the Duvernay Formation (modified from Lyster et al., 2017). Notice the match between the induced earthquakes, seismogenic wells and the overpressured areas in the Duvernay Fm. The dashed black lines show the margin of the Simonette and Bigstone Leduc Reefs.

simplicity, we defined two sections in the seismogenic area, sections X and Y), centered in the Western and Eastern regions of the cluster of induced events respectively, and another section in a nearby non-seismogenic area, section Z, located 10 km west of Fox Creek (Figure 7).

Table 1 summarizes the estimated reservoir and stress properties for the Western and Eastern clusters (X and Y, respectively) and the non-seismogenic section (section Z). The average depth of the Duvernay Fm., the Total Organic Carbon (TOC), and the temperature gradient (T/m) were acquired from the analysis of Lyster et al. (2017) for the defined X, Y, and Z sections. The pore pressure gradient (P_0/m), the vertical stress gradient (S_V/m), and the minimum horizontal stress gradient (S_h/m) were obtained from the analysis of Shen et al. (2018). The estimated

Table 1
Reservoir and Stress Properties of the Duvernay Fm. in Selected Seismogenic and Non-Seismogenic Areas

Duvernay reservoir properties	Western cluster (section X)	Eastern cluster (section Y)	Non-seismogenic area (section Z)
Average depth (Lyster et al., 2017)	3,750 m	3,500 m	3,250 m
Total Organic Carbon (Lyster et al., 2017)	3.1%–3.5%	3%–3.3%	2.6%–3%
Temperature gradient (Lyster et al., 2017) and estimated Temperature at reservoir depth	T/m = 25°C/km T = 95°C	T/m = 28°C/km T = 98°C	T/m = 30°C/km T = 97.5°C
Pore pressure gradient (Shen et al., 2018) and estimated Pore pressure at reservoir depth	P_0/m = 16–20 kPa/m P_0 = 60–75 MPa	P_0/m = 16–18.5 kPa/m P_0 = 56–64.8 MPa	P_0/m = 14–16 kPa/m P_0 = 45–52 MPa
Vertical stress gradient (Shen et al., 2018) and estimated vertical stress at reservoir depth	S_V/m = 24–25 kPa/m S_V = 90–94 MPa	S_V/m = 24–25 kPa/m S_V = 84–87.5 MPa	S_V/m = 24–25 kPa/m S_V = 78–81 MPa
Minimum horizontal stress gradient (Shen et al., 2018) and estimated minimum horizontal stress at reservoir depth	S_h/m = 20–23 kPa/m S_h = 75–86 MPa	S_h/m = 18.5–20 kPa/m S_h = 64.8–70 MPa	S_h/m = 18–20 kPa/m S_h = 59–65 MPa
Estimated effective horizontal stress at reservoir depth	$S_{h,\mathrm{eff}}$ = 0–26 MPa	$S_{h,\mathrm{eff}}$ = 0–14 MPa	$S_{h,\mathrm{eff}}$ = 7–20 MPa

Temperature (T), Pore pressure (P_0/m), vertical stress (S_V/m), and minimum horizontal stress (S_h/m) at reservoir depth were obtained by multiplying the corresponding gradients with the depth of the Duvernay Fm. in the corresponding section. Finally, the effective horizontal stress at reservoir depth ($S_{h,\text{eff}}$) is given by subtracting the minimum horizontal stress (S_h) and the pore pressure ($S_{h,\text{eff}} = S_h - P_0$). We include ranges for these variables since these quantities are estimates, and the spatial variability should be considered.

We notice increasing overpressure toward the seismogenic area, with pore pressures in the range of 60–75 MPa for section X (Western cluster), 56–64.8 MPa for section Y (Eastern cluster), and 45–52 MPa for section Z (non-seismogenic). The minimum horizontal stress tends to be also higher toward the seismogenic area, with values in the range of 75–86 MPa (section X), and 64.8–70 MPa (section Y) for the seismogenic areas, and 59–65 MPa (section Z) or the non-seismogenic area. However, the effective horizontal stress range toward lower values in the seismogenic area, varying from 0 to 26 MPa (section X) and 0–14 MPa (section Y). These values of effective horizontal stress close to zero might explain why these areas (section X and Y) are more susceptible to failure. In other words, less stress perturbation is required for fault reactivation.

One potential cause to explain the different stress and pore pressures between seismogenic sections (X and Y) and non-seismogenic sections (Z) is the possibility of ongoing hydrocarbon maturation in the seismogenic area. Expansion associated with late-stage gas generation is sufficient to create large overpressures (Hansom & Lee, 2005). Additionally, Eaton and Schultz (2018) argue that the natural decomposition of kerogen has led reservoirs toward failure equilibrium, resulting in an increased likelihood of induced earthquakes. Therefore, ongoing maturation will increase pore pressure and, because of associated volume changes, there could be changes in the minimum and maximum horizontal stresses (Bredehoeft et al., 1994). However, evidence cannot be drawn from temperature and TOC values since they are comparably similar for sections X, Y, and Z.

Another potential explanation for the difference between minimum horizontal stresses in the seismogenic and non-seismogenic sections is the stress amplification due to the presence and topography of the neighboring reefs of the Leduc Fm. When weaker (more compliant) layers are sandwiched between stronger (stiffer) layers, then the variations in material strengths produce stress heterogeneity with different stress magnitudes in each type of layer. Depending on the contrasts in elastic properties, tensile and/or shear failure may occur first in either the strong or weak layers (Langenbruch & Shapiro, 2015; Roche & Van der Baan, 2015). Similarly, the seismogenic area is surrounded by the Simonette and Bigstone Leduc reefs, except for the Northwest region (See Figure 7). This bowl-shaped reef structure, which likely exhibits significant stiffness, may locally change the stress anisotropy and stress magnitudes within the less compliant Duvernay Fm., depending on the distance from the wedge tip, resulting in stress concentration in the area surrounded by the reefs, like section X. This could also explain why section X shows higher values of minimum horizontal stress than nearby non-seismogenic areas.

Multiple studies (Fekadu & Kulhanek, 1994; Hussain et al., 2020) have observed significant spatial variations in the *b*-value, even in proximal regions, resulting in areas with lower *b*-values and higher seismic hazard and other areas with higher *b*-values and lower seismic hazard. This is one of the key observations in the present study, where there is a large difference in seismic hazard between the Eastern and Western sections of the seismic cluster in Fox Creek due to the large difference in their *b*-values (Figure 4). On the other hand, various laboratory and numerical studies (Amitrano, 2003; Goebel et al., 2013; Meredith et al., 1990; Scholz, 2015; Van der Baan & Chorney, 2019) have found that the *b*-values are anticorrelated to the differential stresses σ_1-σ_3, that is, the differential between the maximum (σ_1) and minimum principal stress (σ_3). It is possible that the observed difference in *b*-values between the Eastern and Western sections is a consequence of distinct differential stresses, σ_1-σ_3, among these regions. In particular, we would expect larger differential stress in the Eastern section, resulting in lower *b*-values. It should be noted that the Fox Creek area is considered a region largely dominated by a strike-slipe regime (Shen, Schmitt, & Schultz, 2019; Wang et al., 2017). Therefore, the differential stresses, σ_1-σ_3, are given by the differential between the maximum and minimum horizontal stress, S_H - S_h.

Shen, Schmitt, and Haug (2019) conducted a geomechanical analysis of the Duvernay Fm. in the Fox Creek area, which includes depth profiles of the vertical (S_V) and horizontal stresses (S_H, S_h) estimations and measurements. From these depth profiles, we notice a slight increase in the differential stress, S_H - $S_h \approx$ 50–60 Mpa, around 3,400 and 3,600 m, the approximate depth of section Y (Eastern cluster). This trend is reversed by decreasing differential stress toward greater depths (3,700–4,000 m, S_H - $S_h \approx$ 35 Mpa) and shallower depths (3,000–3,200 m, S_H - $S_h \approx$ 35–45 Mpa), which correspond approximately to the depth of sections X (Western cluster) and Z

(Non-seismogenic), respectively. These estimations of differential stress can give us some indications for the observed variation in *b*-values between these regions since increasing differential stress is related to lower *b*-values. However, we recognize that this trend of increase in the differential stress around 3,400 and 3,600 m is gentle and insufficient to fully explain the different seismogenic properties between the East and West regions. Furthermore, understanding the differences of *b*-values between the Eastern and Western is difficult to determine, and it would require a detailed characterization of the triggered faults in these areas, including their geological properties and analysis of the state of stress. Such analysis is beyond the scope of this study.

6. Conclusions

Retrospective analysis of the annual likelihood of moderate events is an effective instrument to study the evolution of the seismic hazard, particularly in areas with anthropogenic seismic activity. This type of analysis shows the variations in the seismic hazard related to induced seismicity, in this case, as a function of changes in the industrial activity. In the case of Fox Creek, the likelihood of moderate events with magnitudes larger than $M > 4$ has consistently decreased since 2015, from a 95% probability to a 4% probability in 2019 and less than 1% in 2020. This contrasts with the peak in the total volumes and the number of hydraulic fracturing wells per year in the Duvernay Fm., SSO No. 2 area, both occurring in 2019 and 2018, respectively. We believe that this trend in decreasing seismic hazard, which contrasts with increasing human activity, results from a combination of targeting areas less susceptible to induced seismicity, a reduction of the seismic activity in the Eastern region, which exhibited the higher seismic hazard in the area, and changes in the hydraulic fracturing operation strategies implemented by the operators. Furthermore, regulatory implementations like SSO No. 2 have led the operators to exercise precaution in areas with high seismic hazard and implement mitigation strategies if induced seismicity occurs during the hydraulic fracturing stimulation. The case of Fox Creek can be interpreted as an example of how the seismic hazard has been reduced due to collaboration between operators and the regulator.

Data Availability Statement

The AGS earthquake catalog is available through the Alberta Earthquake Dashboard: https://ags-aer.shinyapps.io/Seismicity_waveform_app/. The cumulative monthly injection volumes for the Fox Creek area are included in the Supporting Information. Volume data from individual hydraulic fracturing wells was provided by and is available through the Alberta Energy Regulator.

Acknowledgments
The authors would like to thank Krista Beavis, Steven Lyster, Chris Filewich, Alex McNeil, and Todd Shipman for their constructive and helpful support. Thanks to Virginia Stern for her continuous support in keeping the AGS earthquake catalog up to date. The authors would also like to thank Cornelius Langenbruch and Ryan Schultz for their insightful comments and suggestions on the article.

References

Aki, K. (1965). Maximum likelihood estimate of b in the formula logN=a-bM and its confidence limits. *Bulletin of the Earthquake Research Institute*, *43*, 237–239.

Alberta Energy Regulator. (2015). *Subsurface order no. 2*. [November 2021]. Retrieved from https://www.aer.ca/documents/orders/subsurface-orders/SO2.pdf

Alberta Geological Survey. (2021). Alberta Earthquake Dashboard. [November 2021]. Retrieved from https://ags.aer.ca/data-maps-models/interactive-maps-and-apps/ae

Amitrano, D. (2003). Brittle-ductile transition and associated seismicity: Experimental and numerical studies and relationship with the b value. *Journal of Geophysical Research*, *108*(B1), 2044. https://doi.org/10.1029/2001JB000680

Atkinson, G. M., Eaton, D. W., Ghofrani, H., Walker, D., Cheadle, B., Schultz, R., et al. (2016). Hydraulic fracturing and seismicity in the Western Canada Sedimentary Basin. *Seismological Research Letters*, *87*, 632–647. https://doi.org/10.1785/0220150263

Atkinson, G. M., Ghofrani, H., & Assatourians, K. (2015). Impact of induced seismicity on the evaluation of seismic hazard: Some preliminary considerations. *Seismological Research Letters*, *86*, 1009–1021. https://doi.org/10.1785/0220140204

Baker, J. (2008). *An Introduction to Probabilistic Seismic Hazard Analysis (PSHA)*. Technical Report. [January 2021]. Retrieved from https://web.stanford.edu/~bakerjw/Publications/Baker_(2008)_Intro_to_PSHA_v1_3.pdf

Bredehoeft, J. D., Wesley, J. B., & Fouch, T. D. (1994). Simulations of the origin of fluid pressure, fracture generation, and the movement of fluids in the Uinta Basin, Utah. *AAPG Bulletin*, *78*(11), 1729–1747. https://doi.org/10.1306/a25ff279-171b-11d7-8645000102c1865d

Chopra, S., Sharma, R. K., Ray, A. K., Nemati, H., Morin, R., Schulte, B., & D'Amico, D. (2017). Seismic reservoir characterization of Duvernay shale with quantitative interpretation and induced seismicity considerations—A case study. *Interpretation*, *5*(2), T185–T197. https://doi.org/10.1190/INT-2016-0130.1

Cornell, C. (1968). Engineering seismic risk analysis. *Bulletin of the Seismological Society of America*, *58*, 1583–1606. https://doi.org/10.1785/bssa0580051583

Davis, M., & Karlen, G. (2013). *A regional assessment of the Duvernay Formation; a world-class liquids-rich shale play, GeoConvention 2013: Integration*. 6–10.

Eaton, D. W., Igonin, N., Poulin, A., Weir, R., Zhang, H., Pellegrino, S., & Rodriguez, G. (2018). Induced seismicity characterization during hydraulic-fracture monitoring with a shallow-wellbore geophone array and broadband sensors. *Seismological Research Letters*, *89*, 1641–1651. https://doi.org/10.1785/0220180055

Eaton, D. W., & Schultz, R. (2018). Increased likelihood of induced seismicity in highly overpressured shale formations. *Geophysical Journal International*, *214*(1), 751–757. https://doi.org/10.1093/gji/ggy167

Eyre, T., Eaton, D., Zecevic, M., D'Amico, D., & Kolos, D. (2019). Microseismicity reveals fault activation before Mw 4.1 hydraulic-fracturing induced earthquake. *Geophysical Journal International*, *218*, 534–546. https://doi.org/10.1093/gji/ggz168

Fekadu, K., & Kulhanek, O. (1994). Spatial and temporal variations of b-values along the East African rift system and the southern Red Sea. *Physics of the Earth and Planetary Interiors*, *83*, 249–264.

Goebel, T. H. W., Schorlemmer, D., Becker, T. W., Dresen, G., & Sammis, C. G. (2013). Acoustic emissions document stress changes over many seismic cycles in stick-slip experiments. *Geophysical Research Letters*, *40*, 2049–2054. https://doi.org/10.1002/grl.50507

Ground Water Protection Council and Interstate Oil and Gas Compact Commission. (2021). *Potential induced seismicity guide: A resource of technical & regulatory considerations associated with fluid injection* (Second ed., p. 250). Ground Water Protection Council.

Gulia, L., & Wiemer, S. (2019). Real-time discrimination of earthquake foreshocks and aftershocks. *Nature*, *574*(7777), 193–199. https://doi.org/10.1038/s41586-019-1606-4

Gutenberg, B., & Richter, C. (1944). Frequency of earthquakes in California. *Bulletin of the Seismological Society of America*, *34*, 591–610. https://doi.org/10.1785/bssa0340040185

Hager, B. H., Dieterich, J., Frohlich, C., Juanes, R., Mantica, S., Shaw, J. H., et al. (2021). A process-based approach to understanding and managing triggered seismicity. *Nature*, *595*, 684–689. https://doi.org/10.1038/s41586-021-03668-z

Hajati, T., Langenbruch, C., & Shapiro, S. A. (2015). A statistical model for seismic hazard assessment of hydraulic-fracturing-induced seismicity. *Geophysical Research Letters*, *42*, 10601–10606. https://doi.org/10.1002/2015GL066652

Hansom, J., & Lee, M.-K. (2005). Effects of hydrocarbon generation, basal heat flow and sediment compaction on overpressure development: A numerical study. *Petroleum Geoscience*, *11*, 353–360. https://doi.org/10.1144/1354-079304-651

Hussain, H., Shuangxi, Z., Usman, M., & Abid, M. (2020). Spatial variation of b-values and their relationship with the fault blocks in the western part of the Tibetan Plateau and its surrounding areas. *Entropy*, *22*(9), 1016. https://doi.org/10.3390/e22091016

Kozłowska, M., Brudzinski, M. R., Friberg, P., Skoumal, R. J., Baxter, N. D., & Currie, B. S. (2018). Maturity of nearby faults influences seismic hazard from hydraulic fracturing. *Proceedings of the National Academy of Sciences*, *115*, E1720–E1729.

Langenbruch, C., Dinske, C., & Shapiro, S. A. (2011). Inter-event times of fluid induced earthquakes suggest their Poisson nature. *Geophysical Research Letters*, *38*, L21302. https://doi.org/10.1029/2011GL049474

Langenbruch, C., & Shapiro, S. (2015). Quantitative analysis of rock stress heterogeneity: Implications for the seismogenesis of fluid-injection-induced seismicity. *Geophysics*, *80*, WC73–WC88. https://doi.org/10.1190/geo2015-0061.1

Langenbruch, C., & Zoback, M. D. (2016). How will induced seismicity in Oklahoma respond to decreased saltwater injection rates? *Science Advances*, *2*, e1601542. https://doi.org/10.1126/sciadv.1601542

Lyster, S., Corlett, H. J., & Berhane, H. (2017). Hydrocarbon resource potential of the Duvernay Formation in Alberta – update. In *AER/AGS Open File Report 2017-02*. Alberta Energy Regulator (p. 44).

Meredith, P., Main, I. G., & Jones, C. (1990). Temporal variations in seismicity during quasi-static and dynamic rock failure. *Tectonophysics*, *175*(1-3), 249–268. https://doi.org/10.1016/0040-1951(90)90141-T

Norbeck, J. H., & Rubinstein, J. L. (2018). Hydromechanical earthquake nucleation model forecasts onset, peak, and falling rates of induced seismicity in Oklahoma and Kansas. *Geophysical Research Letters*, *45*, 2963–2975. https://doi.org/10.1002/2017gl076562

Pawley, S., Schultz, R., Playter, T., Corlett, H., Shipman, T., Lyster, S., & Hauck, T. (2018). The geological susceptibility of induced earth- quakes in the Duvernay play. *Geophysical Research Letters*, *45*, 1786–1793. https://doi.org/10.1002/2017gl076100

Reyes Canales, M., & van der Baan, M. (2019). Including non-stationary magnitude-frequency distributions in probabilistic seismic hazard analysis. *Pure and Applied Geophysics*, *176*, 2299–2319. https://doi.org/10.1007/s00024-019-02116-4

Reyes Canales, M., & van der Baan, M. (2020). Are aftershock sequences pertinent to long-term seismic hazard assessments? Insights from the temporal ETAS model. *Journal of Geophysical Research: Solid Earth*, *125*, 237–220. https://doi.org/10.1029/2019JB019095

Reyes Canales, M., & van der Baan, M. (2021). Forecasting of induced seismicity rates from hydraulic fracturing activities using physics-based models for probabilistic seismic hazard analysis: A case study. *Pure and Applied Geophysics*, *178*, 359–378. https://doi.org/10.1007/s00024-021-02661-x

Ries, R., Brudzinski, M. R., Skoumal, R. J., & Currie, B. S. (2020). Factors influencing the probability of hydraulic fracturing-induced seismicity in Oklahoma. *Bulletin of the Seismological Society of America*, *110*, 2272–2282. https://doi.org/10.1785/0120200105

Roche, V., & Van der Baan, M. (2015). The role of lithological layering and pore pressure on fluid-induced microseismicity. *Journal of Geophysical Research: Solid Earth*, *120*, 923–943.

Rodgers, B. (2014). Declining costs enhance Duvernay shale economics. *Oil & Gas Journal*, *112*(9), 70.

Scholz, C. H. (2015). On the stress dependence of the earthquake b value. *Geophysical Research Letters*, *42*, 1399–1402. https://doi.org/10.1002/2014GL062863

Schultz, R., Atkinson, G., Eaton, D. W., Gu, Y. J., & Kao, H. (2018). Hydraulic fracturing volume is associated with induced earthquake productivity in the Duvernay play. *Science*, *359*, 304–308.

Schultz, R., Skoumal, R. J., Brudzinski, M. R., Eaton, D., Baptie, B., & Ellsworth, W. (2020). Hydraulic fracturing-induced seismicity. *Reviews of Geophysics*, *58*.

Schultz, R., & Stern, V. (2015). The Regional Alberta Observatory for Earthquake Studies Network (RAVEN). *CSEG Recorder*, *40*(8), 34–37.

Schultz, R., Wang, R., Gu, Y., Haug, K., & Atkinson, G. (2017). A seismological overview of the induced earthquakes in the Duvernay play near Fox Creek, Alberta. *Journal of Geophysical Research: Solid Earth*, *122*, 492–505.

Shapiro, S., Dinske, C., Langenbruch, C., & Wenzel, F. (2010). Seismogenic index and magnitude probability of earthquakes induced during reservoir fluid stimulations. *Leading Edge*, *29*, 304–309.

Shen, L., Schmitt, D. R., & Haug, K. (2018). Measurements of the states of in situ stress for the Duvernay Formation near Fox Creek, west-central Alberta. In *AER/AGS Report*. Alberta Energy Regulator/Alberta Geological Survey (Vol. 97, p. 29).

Shen, L. W., Schmitt, D. R., & Haug, K. (2019). Quantitative constraints to the complete state of stress from the combined borehole and focal mechanism inversions: Fox Creek, Alberta. *Tectonophysics*, *764*, 110–123.

Shen, L. W., Schmitt, D. R., & Schultz, R. (2019a). Frictional stabilities on induced earthquake fault planes at Fox Creek, Alberta: A pore fluid pressure dilemma. *Geophysical Research Letters*, *46*, 8753–8762. https://doi.org/10.1029/2019GL083566

Shi, Y., & Bolt, B. (1982). The standard error of the magnitude-frequency b-value. *Bulletin of the Seismological Society of America*, *72*, 1677–1687.

Sigman, K. (2013). Non-stationary Poisson processes and Compound (batch) Poisson processes. In *Technical Report*. Columbia Education. Retrieved from http://www.columbia.edu/~ks20/4404-Sigman/4404-Notes-NSP.pdf

Stern, V., Schultz, R., Shen, L., Gu, Y., & Eaton, D. (2013). *Alberta Earthquake Catalogue, Version 1.0: September 2006 through December 2010: AER report*.

van der Baan, M. (2021). Earthquakes triggered by underground fluid injection modelled for a tectonically active oil field. *Nature*, *595*. 655–656.

Van der Baan, M., & Calixto, F. (2017). Human-induced seismicity and large-scale hydrocarbon reduction in the USA and Canada. *Geochemistry, Geophysics, Geosystems*, *18*, 2467–2485. https://doi.org/10.1002/2017GC006915

Van der Baan, M., & Chorney, D. (2019). Insights from micromechanical modeling of intact rock failure: Event characteristics, stress drops and force networks. *Journal of Geophysical Research: Solid Earth*, *124*, 12955–12980. https://doi.org/10.1029/2019JB018121

Van der Elst, N. J. (2021). B-positive: A robust estimator of aftershock magnitude distribution in transiently incomplete catalogs. *Journal of Geophysical Research: Solid Earth*, *126*, e2020JB021027. https://doi.org/10.1029/2020JB021027

Waldhauser, F. (2001). HypoDD: A computer program to compute double-difference earthquake locations. In *USGS Open File Report* (Vol. 01–113, p. 25).

Waldhauser, F., & Ellsworth, W. L. (2000). A double difference earthquakes location algorithm: Method and application to the northern Hayward fault. *Bulletin of the Seismological Society of America*, *90*, 1353–1368.

Wang, R., Gu, Y. J., Schultz, R., Zhang, M., & Kim, A. (2017). Source characteristics and geological implications of the January 2016 induced earthquake swarm near Crooked Lake, Alberta. *Geophysical Journal International*, *210*(2), 979–988.

Weissenberger, J. A., & Potma, K. (2001). The Devonian of western Canada—Aspects of a petroleum system: Introduction. *Bulletin of Canadian Petroleum Geology*, *49*(1), 1–6. https://doi.org/10.2113/gscpgbull.49.1.1

Wiemer, S., & Wyss, M. (1997). Mapping the frequency-magnitude distribution in asperities: An improved technique to calculate recurrence times? *Journal of Geophysical Research*, *102*, 15115–15128.

Wozniakowska, P., & Eaton, D. W. (2020). Machine learning-based analysis of geological susceptibility to induced seismicity in the Montney Formation, Canada. *Geophysical Research Letters*, *47*, e2020GL089651. https://doi.org/10.1029/2020GL089651

Zhang, F., Yin, Z., Chen, Z., Maxwell, S., Zhang, L., & Wu, Y. (2019). Fault reactivation and induced seismicity during multistage hydraulic fracturing: Microseismic analysis and geomechanical modeling. *SPE Journal*, *25*, SPE-199883-PA.